A source model for earthquakes near the nucleation dimension

Camilla Cattania[1]

[1]Department of Earth, Atmospheric, and Planetary Sciences, Massachusetts Institute of Technology, Cambridge, MA, camcat@mit.edu

Abstract

[1] Earthquake self-similarity is a controversial topic, both observationally and theoretically. Theory predicts a finite nucleation dimension, implying a break of self-similarity below a certain magnitude. While observations of non self-similar earthquake behavior have been reported, their interpretation is challenging due to trade-offs between source and path effects and assumptions on the underlying source model.

Here I introduce a source model for earthquake nucleation and quantify the resulting scaling relations between source properties (far-field pulse duration, seismic moment, stress drop). I derive an equation of motion from fracture mechanics for a circular rupture obeying rate-state friction and a simpler model with constant stress drop and fracture energy. The latter provides a good approximation to the rate-state model, and leads to analytical expressions for far-field displacement pulses and spectra. The onset of ground motion is characterized by exponential growth with characteristic timescale $t_0 = R_0/v_f$, with R_0 the nucleation dimension and v_f a limit rupture velocity. Therefore, normalized displacements have a constant duration, proportional to the nucleation length rather than the source dimension. For ray paths normal to the fault, the exponential growth results in a Boatwright spectrum with $n = 1$, $\gamma = 2$ and corner frequency $\omega_c = 1/t_0$. For other orientations, the spectrum has an additional sinc$(\cdot)$ term with a corner frequency related to the travel time delay across the asperity. Seismic moments scale as $M_0 \sim R(R - R_0)R_0$, where R is the size of asperity, becoming vanishingly small as Rrightwards arrow R0. Therefore, stress drops estimated from M_0 and f_c are smaller than the nominal stress drop, and they increase with magnitude up to a constant value, consistent with several seismological studies. The constant earthquake duration is also in agreement with reported microseismicity: for $0 < M_w < 2$ events studied by Lin et al. (2016) in Taiwan, the observed durations imply a nucleation length between $45 - 80$m.

[1]The authors acknowledge there are no conflicts of interest recorded.

1 Introduction

The concept of earthquake self-similarity (Aki, 1967) is often assumed in seismology, and it is supported by a large body of observations indicating that the stress drop remains constant over a wide range of magnitudes (e.g. Abercrombie, 1995, 2021, and references therein). In contrast, observations suggesting a break in self-similarity have been reported in local studies (e.g. Harrington & Brodsky, 2009; Bouchon et al., 2011; Lin et al., 2016; Imanishi & Uchide, 2017; Trugman & Shearer, 2017; H. Wang, Ren, Wen, & Xu, 2019; Mayeda, Malagnini, & Walter, 2007; Bindi, Spallarossa, Picozzi, & Morasca, 2020), even though their interpretation is hampered by well known artifacts due to trade-offs between path and source effects and attenuation of high-frequencies (Abercrombie, 1995; Ide, Beroza, Prejean, & Ellsworth, 2003; Abercrombie, 2021).

Scale invariance typically arises from physical processes without a characteristic length scale. In contrast, laboratory constrained friction laws exhibit a characteristic slip distance that determines the weakening behavior. This results in characteristic lengths which have been derived based on fracture energy arguments (Palmer & Rice, 1973; Andrews, 1976; Rubin & Ampuero, 2005) and linear stability analysis (Ruina, 1983). The existence of nucleation length was confirmed in numerical studies of faults with rate-state friction (Dieterich & Linker, 1992; Rubin & Ampuero, 2005), and observed experimentally (Leeman, Saffer, Scuderi, & Marone, 2016; McLaskey, 2019; Ohnaka & Shen, 1999; Latour, Schubnel, Nielsen, Madariaga, & Vinciguerra, 2013).

Self-similarity is often inferred from the scaling between seismic moment and corner frequency. The seismic moment produced by a circular rupture of radius R and stress drop $\Delta\tau$ is given by (Eshelby, 1957; Keilis-Borok, 1959):

$$M_0 = \frac{16}{7}\Delta\tau R^3. \tag{1}$$

Assuming that the earthquake duration T scales linearly with its radius, and taking the corner frequency $f_c \propto 1/T$ leads to the predicted the scaling: $M_0 \propto f_c^{-3}$. A significant source of uncertainty is the constant of proportionality between corner frequency and source dimension, which strongly depends on the chosen source model. Self-similar models, such as those proposed by Madariaga (1976) and Sato and Hirasawa (1973), assume that ruptures start at the center of a circular asperity and propagate at constant velocity. Recent studies have relaxed some of these assumptions, by considering the effect of a cohesive zone (Kaneko & Shearer, 2014), elliptical and unilateral rupture propagation (Kaneko & Shearer, 2015), irregular ruptures on heterogeneous faults (Lin & Lapusta, 2018) and earthquakes propagating as pulses rather than cracks (Y. Wang & Day, 2017). These factors introduce variability in estimating the source dimension, which can strongly affect stress drop estimates due to the cubic dependence on R in eq. 1. Several authors studied the acceleration phase associated with a finite nucleation dimension (e.g. Campillo & Ionescu, 1997; Sato & Kanamori, 1999), but the implication of these results for scaling

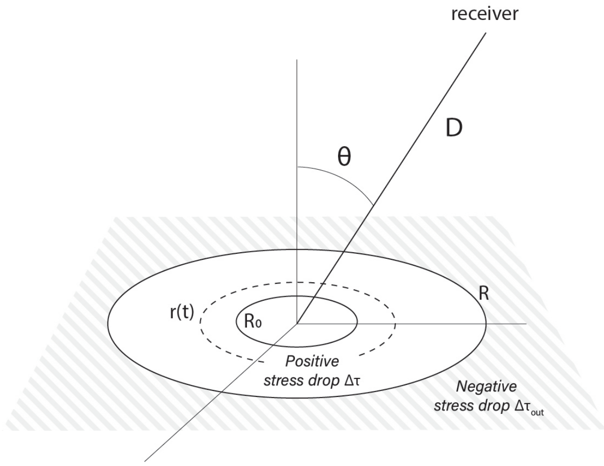

Figure 1: Coordinate system and sketch of rupture propagation. Circular ruptures propagate at variable speed into a region of positive stress drop ($r < R$) and arrest due to a negative stress drop at $r > R$. R_0 is a nucleation radius defined in the text.

relations and the magnitude dependence in inferred stress drops remain unclear.

Here I use fracture mechanics to derive a kinematic source model that accounts for earthquake nucleation, and describe its predictions for seismological observables such as far-field displacement pulse duration and stress drop estimates. I consider two cases: a simple model with constant stress drop and fracture energy; and rate-state friction, which introduces a dependence of fracture energy and stress drop on slip velocity. Both models predict an apparent constant source duration for small earthquakes, as confirmed by fully dynamic rupture simulations. Assuming constant stress drop and fracture energy, I show that the spectrum is characterized by two corner frequencies, associated with source and path effects. In section 3 I discuss these findings in the context of seismological studies, and show that the model can explain observations of constant source duration (Lin et al., 2016; Harrington & Brodsky, 2009; Lengliné, Lamourette, Vivin, Cuenot, & Schmittbuhl, 2014) with a nucleation dimension of the order of $45-80$m. The model also predicts an increase in stress drop with magnitude, as inferred in several studies (Mayeda et al., 2007; Bindi et al., 2020; Trugman & Shearer, 2017, among others). Other predictions, such as the double corner frequency and its dependence on observation angle, may be used to further test this hypothesis and provide estimates of the nucleation dimension in the future.

2 Theoretical source model

To estimate far-field displacement pulses for earthquakes near the nucleation dimension we need an equation of motion for the rupture front, which can be derived from fracture mechanics. I assume a circular crack with uniform, but potentially time-varying, stress drop $\Delta\tau$, radius $r(t)$ and rupture velocity $v_r(t) = \dot{r}$, surrounded by a region of coseismic stress increase which causes the rupture to arrest (Fig. 1)

The motion of the rupture front is controlled by a balance between fracture energy and the mechanical energy provided by slip within the crack (Freund, 1990):

$$G(r, v_r) = \Gamma, \tag{2}$$

where Γ is the fracture energy and G the dynamic energy release rate, which is a function of the its radius and propagation velocity. G is related to the dynamic stress intensity factor K, which quantifies the stress concentration ahead of the rupture, by

$$G = A(v_r)\frac{K(r, v_r)^2}{2\mu'}, \tag{3}$$

where A is a universal function of crack speed (different for each mode of deformation) and μ' is the shear modulus μ for antiplane deformation and $\mu/(1-\nu)$, with ν the Poisson's ratio, for plane strain deformation. The dynamic stress intensity factor can be written as

$$K(r, v_r) = k(v_r)K(r, 0), \tag{4}$$

where $K(r, 0)$ is the static stress intensity factor and $k(v_r)$ a universal function of rupture velocity. To simplify notation, I write the static stress intensity factor as $K(r)$, and rewrite eq. 2 as

$$K(r) = \left(\frac{2\mu'\Gamma}{A(v_r)k(v_r)^2}\right)^{1/2}. \tag{5}$$

The product $A(v_r)k^2(v_r)$ can be approximated as $1 - v_r/v_f$, where v_f is the terminal rupture velocity (shear wave velocity for mode III cracks and the Rayleigh wave velocity for mode II cracks, Freund (1990)). For simplicity, in what follows I neglect the difference between mode II and mode III, and assume that the crack is circular; the same results, within a factor of order one, are expected to apply for the elliptical crack in the case of mixed-mode propagation. The stress intensity factor for a circular crack of radius r is $K(r) = 2\Delta\tau\sqrt{r/\pi}$, and the equation of motion of the crack tip is:

$$r = \frac{\pi}{2}\frac{\mu'}{1 - v_r/v_f}\frac{\Gamma}{\Delta\tau^2}. \tag{6}$$

Fracture energy and stress drop are not, in general, constant. For rate-weakening friction, the stress drop increases with slip velocity. Γ also increases with slip velocity within the crack (Rubin & Ampuero, 2005; Ampuero & Rubin, 2008), and observational studies suggests that Γ increases with slip (Abercrombie & Rice, 2005; Viesca & Garagash, 2015). Therefore I consider two models: one with fracture energy and stress drop increasing during acceleration, consistent with rate-state friction; and one with constant stress drop and fracture energy. I show that as the crack approaches its limit rupture speed, both models are equivalent, and the simpler model has the advantage of providing closed form solutions which can be used to derive analytical expressions for far-field displacement pulses and spectra.

2.0.1 Variable Γ, $\Delta\tau$

In Appendix A I derive expressions for crack growth controlled by rate-state friction; the main results are summarized here. Consider a fault governed by rate-state friction (Marone, 1998, and references therein):

$$\tau_f(v,\theta) = \sigma\left[f_0 + a\ln\frac{V}{V^*} + b\ln\frac{\theta V^*}{d_c}\right], \tag{7}$$

where V is the slip velocity, a, b and are constitutive parameters; d_c is the state evolution distance; σ is effective the normal stress; V^* is a reference slip velocity; f_0 is the steady-state friction coefficient at $V = V^*$, and θ is a state-variable. The state variable evolves according to the ageing law (Ruina, 1983):

$$\frac{d\theta}{dt} = 1 - \frac{\theta V}{d_c}, \tag{8}$$

or the slip law:

$$\frac{d\theta}{dt} = -\frac{V\theta}{d_c}\ln\frac{V\theta}{d_c}. \tag{9}$$

Both stress drop and fracture energy are a function of slip velocity: stress drop increases logarithmically with V, and fracture energy increases logarithmically with V for the slip law and with the square of the logarithm of V for the aging law (Rubin and Ampuero (2005); Ampuero and Rubin (2008); Appendix A). The rupture velocity is linearly proportional to slip velocity (e.g. Latour et al. (2013); Ampuero and Rubin (2008): $v_r \approx (\mu/\Delta\tau_{p-r})V$, where $\Delta\tau_{p-r}$ is the peak-to-residual stress. Therefore we can obtain expressions for stress drop and fracture energy as a function of rupture velocity, and rewrite 6 as:

$$r = \frac{R_\infty}{1 - v_r/v_f}\left[\frac{\ln v_r/v_c}{\ln v_r/v_{bg}}\right]^2 \tag{10}$$

for the aging law and

$$r = \frac{2R_\infty}{1 - v_r/v_f}\frac{\ln v_r/v_c}{(\ln v_r/v_{bg})^2} \tag{11}$$

for the slip law, where v_c and $v_{bg} < v_c$ are characteristic velocities that control the growth of fracture energy and stress drop with rupture velocity. R_∞ is the aging law nucleation length derived by Rubin and Ampuero (2005) by recognizing that the bracketed term in eq. 10 tends to 1 for sufficiently large slip velocities. In this case, and more generally for any frictional law with constant Γ and $\Delta\tau$, the rupture velocity is simply given by

$$v_r = v_f\left(1 - \frac{R_0}{r}\right). \tag{12}$$

with

$$R_0 = \frac{\pi}{2}\frac{\mu'\Gamma}{\Delta\tau^2}, \tag{13}$$

which is the radius of a stationary crack and corresponds to R_∞ for the aging law.

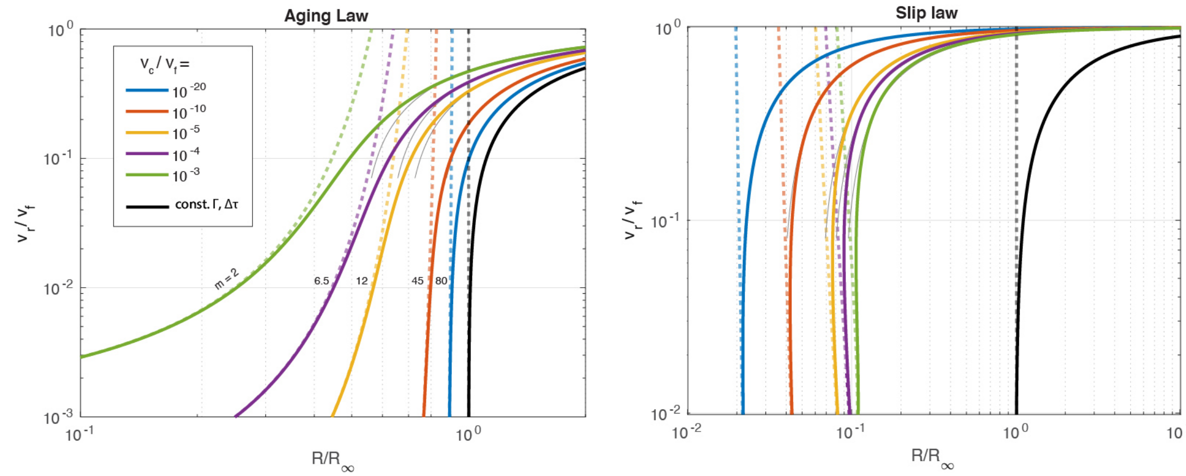

Figure 2: Evolution of rupture velocity with radius for rate-state models with the aging law (left) and slip law (right) for different values of normalized characteristic velocity v_c/v_f; I assumed $v_{bg} = 0.1v_c$ in all cases. Solid lines indicate dynamic models (eq. 10, 11) and dotted lines indicate quasi-static models obtained by setting $v_r/v_f = 0$. For small v_c/v_f, the quasi-static solution approaches R_∞, and dynamic solutions approach the constant model (black). Thin black lines indicate the constant $\Gamma, \Delta\tau$ model shifted along the x-axis, representing the same scaling but with a different nucleation dimension. Numbers indicate the power-law exponent in the relation $v_r \sim r^m$, calculated at $v_r/v_f = 0.01$.

Fig. 2 shows rupture velocity as a function of crack radius for different values of v_c/v_f and assuming $v_{bg} = 0.1v_c$. I also plot the quasi-static solution ($v_r/v_f = 0$; dotted lines). As expected, quasi-static solutions for the aging law approach R_∞ at high slip velocities for small values of v_c/v_f. For the slip law, quasi-static solutions corresponding to an expanding crack do not exist (Ampuero & Rubin, 2008), since the ratio $\Gamma/\Delta\tau^2$ decreases with slip velocity so that the crack radius would have to shrink to maintain energy balance. However, in the dynamic regime we see that crack-like expansion is possible, as shown by the trajectories of increasing velocity with radius. This would suggest that nucleation may start as a unidirectional pulse identified by Ampuero and Rubin (2008), and then evolve into a crack as the rupture velocity approaches around $1-10\%$ of its limit value (based on Fig. 2). Crack-like propagation has in fact been seen in slip law numerical simulations by Kaneko and Ampuero (2011), under different loading conditions from those used by Ampuero and Rubin (2008). Note that the trajectories for crack-like expansion start at $r < R_\infty$, indicating that the nucleation dimension is smaller for the slip law than the aging law, consistent with Ampuero and Rubin (2008).

The evolution of rupture velocity as a function of crack radius can be directly compared with laboratory observations. Ohnaka and Shen (1999) and Latour et al. (2013) identified three rupture stages in laboratory nucleation: 1. a quasi-static phase, in which rupture velocity grows slowly; 2. a nucleation phase characterized by a power-law acceleration ($v_r \sim r^m$), and a dynamic phase with constant rupture velocity. The laboratory observations from Latour et al. (2013) were successfully reproduced in rate-state simulations byKaneko, Nielsen, and Carpenter (2016). Here I find that aging law nucleation model produces a similar behavior, with power law exponent controlled by v_c/v_f (Fig. 2). The slip law model does not produce the power-law growth in Fig. 2, although this was observed in slip-law simulations by Kaneko et al. (2016); it is possible that other values of v_c, v_{bg} may produce the power-law scaling. In what follows, I discuss the relationship between the growth exponent and v_c/v_f, since this parameter is likely to vary by several orders of magnitude between laboratory experiments and nature. Note that the choice of v_{bg}/v_f will also affect m, but the overall trend is not expected to change. I discuss specific the exponent for the aging law model at $v_r/v_f = 0.01$, which falls well into the power-law regime in the laboratory experiments byLatour et al. (2013). As the solution approaches the model with constant $\Delta\tau, \Gamma$ for small v_c/v_f, it becomes increasingly steep; while for $v_c/v_f \approx 10^{-4} - 10^{-3}$, the power law exponent is more consistent to the value observed by Latour et al. (2013) (between 4 and 5) and Ohnaka and Shen (1999) (7.31). In Appendix A I show that $v_c/v_f \approx d_c/(\theta_i V_f)$, where θ_i is the state variable ahead of the crack dip and V_f the slip velocity during the dynamic phase of the earthquake. During the interseismic period, $\dot{\theta} \approx 1$ so that θ can be approximated as the time since the last earthquake. Therefore we expect that a longer interevent time will produce higher growth exponents, as confirmed by experiments carried out at a different loading rates (Figure 9 in Kaneko et al. (2016)). This implies that the model with constant $\Gamma, \Delta\tau$ may not be appropriate for laboratory experiments with an interevent time of the order of seconds-minutes and $m < 10$, but it is a good approximation for tectonic events with recurrence intervals of the order of days to centuries and likely much higher growth exponents than those observed in the laboratory. For example, taking $d_c = 100\mu$m, $V_f = 1$m/s and θ between 1 day and 100 years (representative of small moderate earthquakes respectively) yields $v_c/v_f \approx 10^{-9} - 10^{-14}$, which are indistinguishable from the model with constant $\Gamma, \Delta\tau$. Therefore, in the rest of the paper I primarily focus on this model, which is mathematically more tractable.

2.0.2 Solutions for constant Γ, $\Delta\tau$

Since $\dot{r}(R_0) = 0$, solving for crack position as a function of time with initial condition $r(0) = R_0$ gives $r(t) = R_0$ at all times. Instead, I assume that the crack exceeds the nucleation dimension by a small amount: $r/R_0 = 1 + \epsilon$, with $\epsilon \ll 1$. The solution to eq. 12, obtained in Mathematica (Wolfram Research, 2022) and discovered by (Barry, Parlange, Sander, & Sivaplan, 1993), is as follows:

$$r/R_0 = 1 + W\left(ge^{t/t_0}\right) \quad (14)$$

$$v_r/v_f = 1 - \left[1 + W\left(ge^{t/t_0}\right)\right]^{-1} \quad (15)$$

where $W(\cdot)$ is the Lambert omega function, $t_0 = R_0/v_f$ is a characteristic timescale, and $g =$

$W^{-1}(\epsilon) \approx \epsilon$.

The same energy arguments can be applied to rupture arrest by introducing a region of negative stress drop for $r > R$, and modifying the stress intensity factor accordingly (see Appendix B). This is analogous to assuming a rate-strengthening friction outside the asperity. I find that rupture arrest has a minor effect on source properties (Fig. A1) for sufficiently strong rupture barriers. Unless otherwise specified, in the rest of the paper I show simulations for a stress increase equal and opposite to the stress drop, and I neglect rupture arrest when deriving analytical results.

2.1 Far-field pulses and amplitude spectra

The kinematic source models presented above are the starting point to find far-field ground motion and source spectra for an accelerating crack. Far-field pulses and spectra are obtained from body wave displacements for a point source shear dislocation (Aki & Richards, 1980):

$$\mathbf{u}(\mathbf{x}, t) = \frac{\mathbf{A}^{p,s}}{4\pi\rho c_{p,s}^3 D} \dot{M}_0\left(t\right), \tag{16}$$

where ρ is the density, $c_{p,s}$ is the wave velocity for P or S waves, $\mathbf{A}^{p,s}$ the respective radiation patterns, D is the distance between source and receiver, and $\dot{M}_0$ the moment rate given by

$$\dot{M}_0(t) = \mu \int\int_s V\left(t - d/c_{p,s}\right)\, ds, \tag{17}$$

with μ the shear modulus, V the slip velocity, and d the distance between the receiver and individual points on the fault surface s. A constant stress drop crack propagating at speed v_r has the following velocity profile:

$$V(\tilde{r}) = \frac{24\Delta\tau}{7\pi\mu} \frac{r(t)}{\sqrt{r(t)^2 - \rho^2}} v_r(t), \tag{18}$$

where $\Delta\tau$ is the stress drop, $r(t)$ the crack radius, and ρ radial distance within the crack (Sato & Hirasawa, 1973).

For $\theta = 0$, and neglecting rupture arrest, I calculate normalized moment rates as the product $\Delta\tau r v_r$, using eq. 15 for the constant Γ model and solving eq. 6 using the matlab function ode15i (Fig. 3). All subsequent figures include rupture arrest, in which case I use the equation of motion derived in Appendix B.

Equipped with the rupture front equation of motion (eq. 15), in the following sections I present analytical expressions for far-field displacements pulses and spectra. For mathematical tractability, I neglect rupture arrest. A particularly simple solution can be obtained for $\theta = 0$, since far-field displacements are proportional to the average moment rate and the only timescale in the solution is associated with the source process (section 2.1.1). For all other angles, we find a two timescales, associated with source and path effects (section 2.1.2).

Table 1: Notation.

Symbol	Definition
G	energy release rate
Γ	fracture energy
$K(r, \dot{r})$	dynamic stress intensity factor
$K(r)$	static stress intensity factor
μ'	μ for antiplane strain, $\mu/(1-\nu)$ for plane strain (μ = shear modulus, ν = Poisson's ratio)
$r(t)$	instantaneous rupture radius
v_r	$\dot{r}$; instantaneous rupture velocity
v_f	final rupture velocity ($r \to \infty$)
v_c	characteristic rupture velocity controlling scaling of Γ
v_{bg}	characteristic rupture velocity controlling scaling of $\Delta\tau$
a, b	rate-state parameters
d_c	rate-state state evolution distance
R_0	nucleation radius (eq. 13)
R_∞	rate-state, aging law nucleation radius
R	radius of region with positive stress drop ($\approx$ final earthquake radius)
t_0	R_0/v_f; characteristic nucleation timescale
V	slip velocity
$\Delta\tau$	nominal stress drop (region: $r < R$)
$\Delta\tau_{out}$	stress increase in arrest region ($r > R$)
$\Delta\tau_m$	apparent stress drop (eq.27)
u	far field ground displacement
u_{max}	peak far field displacement
$\dot{M}_0$	moment rate
$c_{p,s}$	P, S wave velocity
θ	observation angle
ϕ	threshold to define pulse duration: $u \geq \phi u_{max}$
T	half-duration of far-field pulse
Θ	$R \sin\theta / ct_0$
f_c	corner frequency
$M_{0,ref}$	$(16/7)\Delta\tau R_0^3$; reference seismic moment
$M_{w,ref}$	reference moment magnitude, corresponding to $M_{0,ref}$
ω_c	$1/t_0$, characteristic corner frequency
n, γ	exponents in Boatwright (1978) model

2.1.1 Pulses and spectra for $\theta = 0$

In Fig. 3 I compare normalized far-field spectra from dynamic rupture simulations with the model of Sato and Hirasawa (1973) (which assumes constant rupture velocity) and the two aging law rupture model introduced in the previous section.

Both models are simplified representations of the more complex elasto-frictional processes taking place during nucleation and rupture propagation, and they contains several assumptions. Therefore, I also run fully dynamic rupture simulations of earthquake cycles on faults controlled by rate-state friction with the ageing law, using the numerical code of Lapusta et al. (2009), described in Appendix C, and compare far-field pulses with the nucleation models. As expected, the classic model assuming constant rupture velocity produces far-field displacement pulses of increasing duration with increasing earthquake dimension R. In contrast, the accelerating models produces longer pulses due to the slower average rupture velocity, and with approximately constant duration. The rate-state, aging law model produces very similar far-field ground motion as the constant Γ, $\Delta\tau$ model, consistent with the results from section 2.0.1: accounting for variable fracture energy and stress drop only affects crack growth at low rupture velocities, when the $\sqrt{1 - v_r/v_f}$ term is negligible and rupture propagation is controlled by dependence of fracture energy and stress drop on v_r. Since here we are interested in events that are fast enough to generate seismic waves, I consider events with $\max(v_f) \geq 0.1 v_f$, and in this regime the two models are virtually indistinguishable.

We also find that dynamic rupture simulations for events with $R_\infty < R < 1.6 R_\infty$, where R_∞ is the nucleation radius ((Rubin & Ampuero, 2005); eq. 39) collapse on the same line and have approximately constant duration as predicted by the analytical model. As previously observed by Chen and Lapusta (2009) and Cattania and Segall (2019), asperities exceeding $R \approx R_{inf}$ tend to produce lateral ruptures, not described by the circular model adopted here. Dynamic simulations exhibit a longer arrest phase, likely caused by the healing wave traveling across the asperity (Madariaga, 1976), not captured by the kinematic models.

The constant duration of far-field displacement pulses is one of the main results of this study. It can be understood from the equation of motion. For the observation angle $\theta = 0$ and in the far field, the time delay in eq. 16 is a constant, so the observed displacement is simply proportional to the integrated slip velocity. It can be shown that the integral is proportional to the product of crack area and rupture velocity:

$$u \sim r(t)^2 v_r(t), \tag{19}$$

where I omitted the constant time delay d/c in eq. 17 for convenience. For constant rupture velocity $v_r = v_f$, far field displacements simply grow as rupture area or t^2. If we redefine time so that $t = 0$ corresponds to the time when the rupture reaches $r = R$ (as in Fig. 3) and normalize the far-field

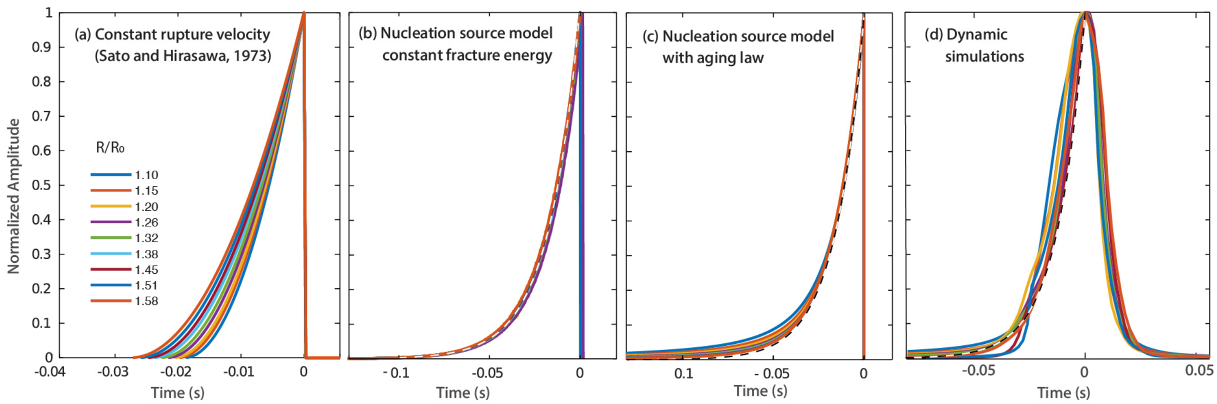

Figure 3: Normalized far-field displacements observed at $\theta = 0$ for different underlying source models. (a) Sato and Hirasawa (1973) model with constant rupture velocity. (b) kinematic modified model accounting for accelerating rupture, with instantaneous rupture arrest and constant fracture energy and stress drop. (c) kinematic model for rate-state friction with the aging law with $v_c/v_f = 10^{-8}$, $v_{bg}/v_f = 10^{-9}$ (eq. 10). (d) fully dynamic earthquake simulations. Dotted lines are theoretical expressions for $R \approx R_0$ ($u/u_{max} = \exp(-\Delta t/t_0)$). The nucleation length R_0 in panels (b,c) is set to R_∞ (eq. 39) corresponding to the parameters in the simulation (Appendix D). The rupture velocity v_r is equal to the shear wave speed, corresponding to the mode III edge of the rupture.

displacement, we obtain:

$$\frac{u}{u_{max}} = \left(\frac{R/v_f - t}{R/v_f}\right)^2. \tag{20}$$

Defining the earthquake half-duration T as the time when far-field displacements reach an arbitrary fraction of its peak value ($u = \phi u_{max}$), we obtain $T = R/v_f(1 - \sqrt{\phi})$: as expected, earthquake duration grows linearly with source dimension.

For the accelerating crack, both r and v_r are time-dependent. Early on, $v_r \approx 0$ and we can assume that the radius is approximately constant, so that far-field displacement is proportional to the rupture velocity given by eq. 15. In the early stages of nucleation, when $ge^{t/t_0} \ll 1$, the Lambert W-function can be approximated as $W(x) \approx x$ for $x \ll 1$ so that $\dot{r}/c \approx ge^{t/t_0}$. Note that this solution can also be derived from eq. 12 with $r \to R_0$. The normalized far-field displacement observed at a time t before the end of the rupture is then simply

$$\frac{u}{u_{max}} = \frac{v_r}{v_{r,\max}} = e^{-t/t_0}, \tag{21}$$

which does *not* depend on the final radius but only on t/t_0, so that all normalized curves collapse on the same line. This expression, shown by the dotted lines in Fig. 3(b,c), is in excellent agreement with both nucleation models and with the dynamic simulations. As before, we define the earthquake half-duration as the time when far-field displacements reach an arbitrary fraction of its peak value ($u = \phi u_{max}$), which gives the event duration

$$T = t_0 \ln\left(\frac{1}{\phi}\right). \tag{22}$$

with $t_0 = \frac{R_0}{v_f}$. Finally, the Fourier transform of eq. 21 produces the following normalized amplitude spectrum:

$$|u(\omega)| = \frac{u_{max} t_0}{\sqrt{1+\omega^2 t_0^2}}, \tag{23}$$

which corresponds to a Boatwright (1978) spectrum as generalized by Abercrombie (1995), with $n = 1$, $\gamma = 2$, and corner frequency $\omega_c = 1/t_0$.

2.1.2 Pulses and source spectra for all observation angles

Displacement pulses and source spectra as a function of observation angle are derived in Appendix C; here I summarize the main results. The pulse half-duration is given by

$$T = t_0 \left[\ln\left(\frac{1}{\phi}\right) + \ln\left(\frac{e^{\Theta} - 2\phi \sinh\Theta}{e^{-\Theta}}\right)\right] \tag{24}$$

with $\Theta = R \sin\theta / c t_0$, c is the speed of P or S waves, R the asperity dimension, and ϕ the threshold defined in section 2.1.1. The first term in square brackets reflects the acceleration in slip velocity during nucleation, and it does not depend on R; the second term is associated with the time lag between radiation from opposite sides of the rupture, which increases with source radius and observation angle.

Finally, the spectrum of the moment rate function is given by

$$|\dot{M}_c(\omega)| = \frac{48\Delta\tau}{7}(R - R_0)R_0 R \,\mathrm{sinc}\left(\frac{\omega R \sin\theta}{c}\right)\frac{1}{\sqrt{\omega^2 t_0^2 + 1}}. \tag{25}$$

The spectrum has two corner frequencies, corresponding to the two characteristic timescales discussed above. The $\mathrm{sinc}(\cdot)$ reflects the travel time difference between opposite ends of the rupture, while the Boatwright term, previously obtained for $\theta = 0$, reflects the exponential increase in rupture velocity (eq. 21), which is a function of nucleation length rather than asperity dimension.

Most seismological studies use a spectrum with a single corner frequency, which will fall between these values. This can be verified by fitting a Brune (1970) and a Boatwright (1980) models to the amplitude spectrum obtained from the nucleation source model (Fig. 4). Corner frequencies f_c and fall-off rates are estimated using a least-square fit weighted by the inverse of the frequency, in the frequency range $0.05 f_c < f < 10 f_c$ (Kaneko & Shearer, 2014). As expected, the Boatwright model correctly describes the spectrum for $\theta = 0$. For larger θ, the Brune model better captures the lower corner frequency (and hence source behavior), while Boatwright estimates are closer to the second corner frequency for small values of θ, up to about 20°.

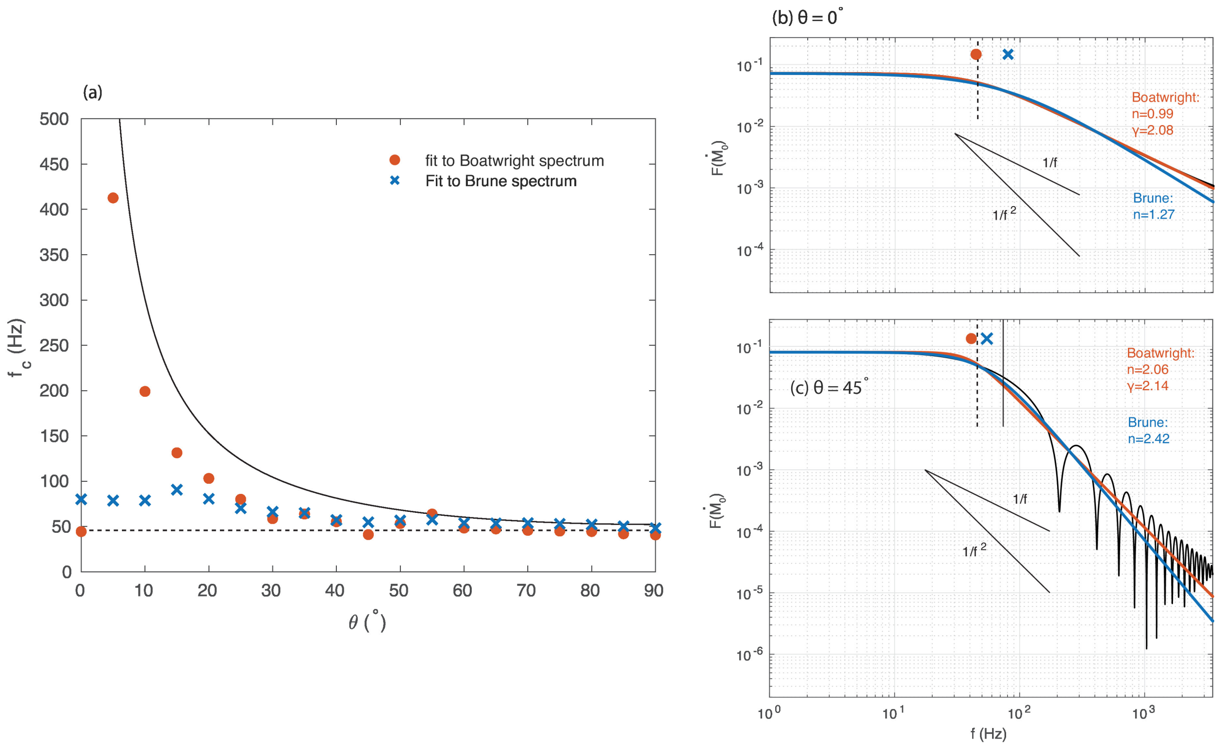

Figure 4: Corner frequency and fall-off exponents estimated by fitting a Brune and a Boatwright spectrum to the far-field displacements produced by an event near the nucleation dimension $R = 1.1R_0$ and fast rupture arrest ($\Delta\tau_{out} = -4\Delta\tau$), with $R_0 = 10$m, $v_f = 2880$m/s. (a) Brune (cross) and Boatwright (circle) corner frequencies generally fall between the two theoretical corner frequencies predicted by eq. 25 associated with the rupture acceleration (dotted line) and to the delay between stopping phases (solid line). (b) Spectrum for $\theta = 0°$, close to the expected Boatwright spectrum for $R \approx R_0$, eq. 23. (c) Spectrum for $\theta = 45°$.

2.2 Seismic moment and stress drop scaling

The seismic moment is estimated from the zero-frequency asymptote of the moment rate function (Aki & Richards, 1980), and shown in Fig. 5(a). Moments are normalized by the moment that a constant stress drop crack of size R_0 would produce if it ruptured seismically: $M_{0,ref} = (16/7)\Delta\tau R_0^3$, and the respective magnitude is denoted by $M_{w,ref}$. While this value does not have an obvious physical interpretation, since eq. 1 does not apply in this limit, I introduce it for convenience, to facilitate interpretation of seismological observations in terms of a nucleation dimension. For sufficiently large asperities ($R \approx 2R_0$ or larger), seismic moments scale follow the classical scaling ($M_0 \sim R^3$, eq. 1); in contrast, the seismic moment for events near the nucleation dimension is lower than the classical result, since slip is released aseismically during the nucleation phase. In this case, seismic moments are given by eq. 25 for $\omega = 0$:

$$M_0 = \frac{48}{7}\Delta\tau R_0 R(R - R_0). \tag{26}$$

Note that the existence of a finite nucleation length does not translate to a lower bound in seismic moment: eq. 26 predicts arbitrarily small M_0, due to a small amount of seismic slip over a finite source.

If corner frequencies are inversely proportional to source dimension, stress drops can be estimated by plotting M_0 vs. f_c, and the term "stress drop" is often used to describe the scaling between these two quantities, even though some authors have argued against this use of the term (Atkinson & Beresnev, 1997). For small sources, the assumption that $f_c \sim R^{-1}$ clearly does not apply, as confirmed by the constant source duration for small θ (section 2.1.1). For easier comparison with observational studies, I define the measured stress drop as

$$\Delta\tau_m = \frac{7}{16}\frac{M_0 f_c^3}{k^3 c^3}, \tag{27}$$

where k is a constant of proportionality defined by the relationship $\bar{f}_c = kc_s/R$, where $\bar{f}_c$ is the corner frequency averaged over the focal sphere. The value of k depends on assumptions about the source model; here I use $k = 0.21$, the value obtained by Madariaga (1976) for S-waves from dynamic simulations with constant rupture velocity $v_r = 0.9c_s$. This choice affects the absolute value of stress drop estimates, but not its scaling with source dimension or magnitude.

I define corner frequencies as $f_c = 1/(4\pi T)$, where T is time during which $u \geq 0.5u_{max}$, as before. Fig. 5(b) shows the measured stress drop for $\theta = 0$ and $\theta = 45°$: since the source duration tends to a constant for $R \to R_0$, while seismic moments become vanishingly small, estimated stress drops are lower for small magnitude events. This effect is visible for events with moment magnitudes up to about $M_{w,ref} + 2$, at which point $\Delta\tau_m$ approaches a constant value.

3 Discussion

A finite nucleation dimension implies a break in self-similarity, and the traditional scaling relations between seismic moment and earthquake duration (or equivalently, stress drop) are not expected to hold for source dimensions close to the nucleation length. A departure from self-similarity, if observed, could therefore provide an indirect in-situ estimate of the nucleation dimension, and a comparison to laboratory or numerical experiments under which earthquake nucleation has been hypothesized and observed (Dieterich, 1992; McLaskey, 2019). Here I presented a simple analytical source model for events near the nucleation dimension, and outline seismological observations and scaling relations that might reveal a break in self-similarity.

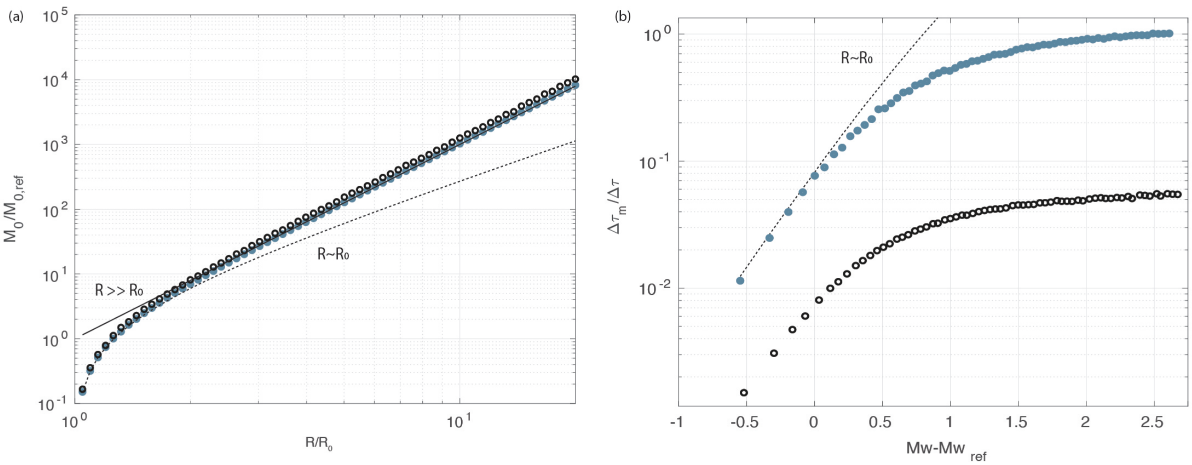

Figure 5: (a) normalized seismic moment vs. normalized radius predicted by the theoretical source model (section 2). The solid and dotted lines indicate analytical results for $R \gg R_0$ (eq. 1) and $R \approx R_0$ (eq. 26). Light blue, solid circles are the $\theta = 0°$; black empty circles for $\theta = 45°$. (b) Measured stress drop vs. earthquake magnitude.

Like all source models assuming a circular rupture propagating on a uniform fault, this model doesn't capture the complexity of real earthquakes, which can have complex source time functions even at small magnitude (Abercrombie, 2021) and increased variability in stress drop due to rupture geometry and other factors (Kaneko & Shearer, 2014, 2015; Lin & Lapusta, 2018; Y. Wang & Day, 2017).

But while the model will not capture all details of real earthquakes, the existence of a finite nucleation dimension fundamentally modifies source properties and scaling relations, and these first-order features likely persist in more realistic cases. In particular, the constant duration of far-field displacement pulses appears to be a robust feature, common to models with constant or variable fracture energy (Fig. 3). This is likely to be the case for other frictional mechanisms in which the ratio $\Gamma/\Delta\tau^2$ scales weakly with slip velocity as the rupture approaches the dynamic regime.

3.1 Comparison with earlier studies

The source model with constant fracture energy is qualitatively similar to the one proposed by Sato and Kanamori (1999), who also used a Griffith criterion to model crack growth. Instead of assuming a uniform stress drop, they modeled a rupture propagating into the stress field induced by the pre-existing crack. In their model, velocities exhibit a similar growth towards a limit value with increasing radius, and the nucleation phase has a duration proportional to $t_0 = R_0/v_f$. Campillo and Ionescu (1997) studied earthquake nucleation by considering the initiation of an elasto-dynamic instability on a slip weakening antiplane interface subject to a sudden perturbation. They identified a nucleation length given by

$$L_n = \frac{\pi \mu L_c}{\Delta\tau^{p-r}}, \tag{28}$$

where L_c is the slip weakening distance, $\Delta\tau^{p-r}$ is the peak to residual stress drop, and a nucleation timescale proportional to L_n/c. This is analogous, but not identical, to our definition of R_0: for slip weakening friction, $\Gamma = \tau^{p-r} L_c/2$ and R_0 in the constant Γ model and is given by eq. 5 for $v_r = 0$:

$$R_0 = \frac{\pi}{4} \frac{\mu' \Delta\tau^{p-r} L_c}{\Delta\tau^2}, \tag{29}$$

which is the same expression derived by Palmer and Rice (1973) and Andrews (1976). In the context of rate-state friction, the length scales L_n and R_0 are related to L_b (Dieterich, 1994) and L_∞ (Rubin & Ampuero, 2005).

3.2 Observations of constant earthquake duration

The first result of this study is that earthquakes near the nucleation dimension appear to have constant duration, given by eq. 24. This perhaps surprising result arises from the early exponential acceleration in rupture velocity, and from the definition of "duration" as the time during which the far-field pulse exceeds a fraction of the final value. Constant earthquake duration across a range of magnitudes has indeed been reported for small events by several authors: Harrington and Brodsky (2009) for microearthquakes along the San Andreas and secondary faults, Lin et al. (2016) for repeaters along the Chengdu fault in Taiwan and Lengliné et al. (2014) for fluid induced earthquakes. Lin et al. (2016) estimated earthquake durations from source time functions, and defined them as twice the time during which the moment rate exceeds 50% of the peak value. These observations can be directly compared to the prediction from eq. 24 and seismic moments from eq. 26, as shown in Fig. 6. The nucleation model provides a better fit that the classical scaling, and can explain the observed source duration with a nucleation dimension of the order of about $45-80$m.

3.3 Observations of magnitude dependent stress drops

Evidence for breaks in self-similarity in larger datasets remains a subject of intense debate (for a review, see Abercrombie (2021)). When estimates of corner frequencies and seismic moment are plotted together for several datasets, stress drops appear to be remarkably constant across a broad range of magnitude, including millimeter scale events recorded in laboratory (Selvadurai, 2019; Yoshimitsu, Kawakata, & Takahashi, 2014), centimeter scale earthquakes in deep mines (Kwiatek & Ben-Zion, 2013), up to kilometer scale earthquakes (e.g. Baltay, Ide, Prieto, and Beroza (2011); Zollo, Orefice, and Convertito (2014); Abercrombie (2021) and references therein). However, observed stress drops span several orders of magnitude, and individual studies have reported trends of increasing stress drops with magnitude in Italy

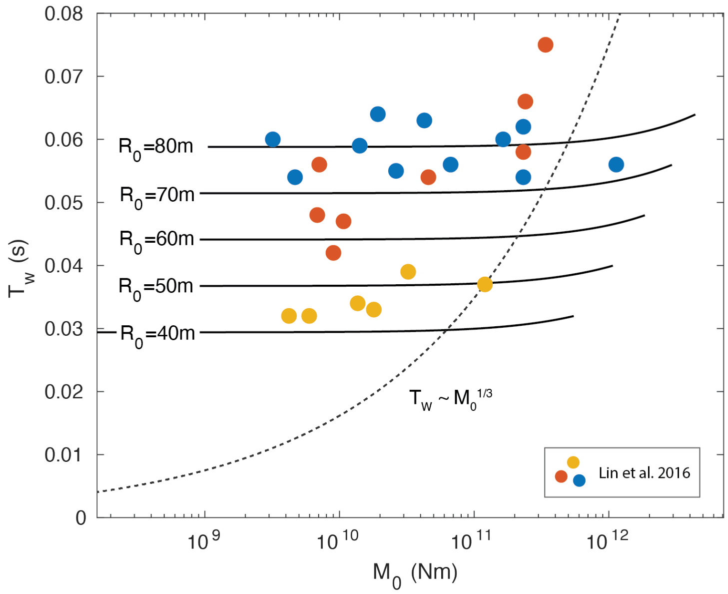

Figure 6: Far-field displacement durations and seismic moments from Lin et al. (2016), with each color corresponding to a different cluster. Black lines indicate the predicted scaling for sources near the nucleation dimension (eq. 24, 26) with $\theta = 28°$, $v_r = 2505$m/s, $c = 5700$m/s, $\phi = 1/2$ (from Lin et al. (2016)), $\Delta\tau = 3$MPa and $\mu = 30$GPa. The dotted line indicates the classical $T \sim M_0^{1/3}$ scaling for a 3MPa stress drop.

(Bindi et al., 2020; H. Wang et al., 2019; Malagnini, Scognamiglio, Mercuri, Akinci, & Mayeda, 2008) and California (Mayeda et al., 2007; Trugman & Shearer, 2017), among others; a consistent observation across many studies is the increased scatter in stress drop for small magnitude earthquakes. These observations are notoriously difficult due the trade-off between source and path effects, including frequency and depth dependent attenuation (e.g. Abercrombie, 1995; Shearer, Abercrombie, Trugman, & Wang, 2019), and hence it remains unclear whether the observed decrease in stress drop for small earthquakes is a source or a path effect.

With these caveats in mind, it is worth noting that theoretical source model presented here provides an explanation for the reported deviations from the $M_0 \sim f_c^{-3}$ scaling, as well as the increase in scatter for small magnitude events. Since a fraction of slip is released aseismically during the nucleation phase, asperities close to the nucleation dimension have smaller seismic moment than predicted by the classical scaling. This effect, combined with the constant duration for small events, reduces stress drops by a factor of about 100 over 2 earthquake magnitudes (Fig. 5). The shape of the curve differs from reported observations, in which the trend persists up to large magnitudes and takes the form: $M_0 \sim f_c^{-(3+\epsilon)}$ (Kanamori & Rivera, 2004). The model could be better reconciled with the data, and reproduce its scatter, by accounting for spatial heterogeneity in nucleation length. I test this idea with a simple syn-

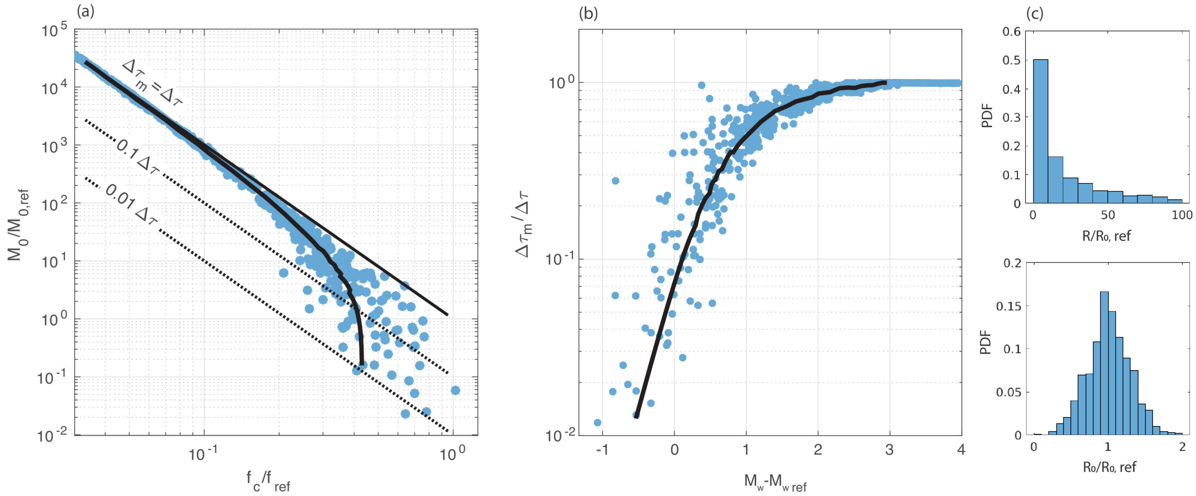

Figure 7: (a) Normalized seismic moment vs. normalized corner frequency, obtained from the scaling shown in Fig. 5 (lines) with variable nucleation lengths drawn from a Gaussian distribution. The reference corner frequency is defined from eq. 27 such that $\Delta\tau_m(M_{0,ref}, f_{ref}) = \Delta\tau$, with $\Delta\tau$ the nomimal stress drop. (b) Ratio between measured and true stress drop vs. magnitude relative to the reference magnitude. (c) PDF of normalized asperity dimensions (top) and nucleation lengths (bottom).

thetic test. I start with a set of 1000 source radii randomly sampled from a uniform distribution in log-space; and a random sample of nucleation dimensions drawn from a Gaussian distribution centered at the reference nucleation dimension R_0, with a standard deviation equal to $0.3R_0$. This produces pairs of source-dimension and nucleation dimensions. I discard pairs with a nucleation dimension exceeding the source radius, since they would be aseismic (Chen & Lapusta, 2009; Cattania & Segall, 2019). For the remaining pairs, I obtain duration and moment by interpolating Fig. 5, and rescaling the result by the characteristic duration and moment for each the nucleation length. Given the scatter in the resulting plots (Fig. 7), it seems plausible that the trend would be interpreted as $M_0 \sim f_c^{-(3+\epsilon)}$, especially if low magnitude events are below the completeness magnitude and hence missing from the catalog. The model also predicts more stress drop variability at low magnitudes, consistent with observations.

To determine whether a finite nucleation dimension causes the observed non-similar scalings, other model predictions could be tested against data. For events with $\theta = 0$, the constant source duration produces constant corner frequency, and the spectrum takes the form of a Boatwright spectrum (eq. 23). For all other observation angles, the Boatwright spectrum is multiplied by a $\mathrm{sinc}(\cdot)$ term corresponding to the delay between phases emitted simultaneously from opposite ends of the source. Should these patterns be discernible in the data, they would corroborate the hypothesis that the existence of a finite nucleation dimension is responsible for observed breaks in self-similarity.

4 Conclusion

I introduce analytical source models accounting for acceleration in slip and rupture velocity as well as the finite size of the nucleation region. In the early phases of nucleation, the model predicts that far field displacements grows exponentially with time, producing a constant source duration and corner frequency. This is consistent with some observations of both tectonic and induced microseismicity, and implies a nucleation dimension of the order of tens of meters. Furthermore, the seismic moment decreases as more slip is accrued aseismically, causing a decrease in estimated stress drop. With the improvement of seismic networks and detection algorithms, future studies may be able to further verify these findings and test additional model predictions, such as the double corner frequency and variations of spectral properties with observation angle.

A Rupture evolution with rate-state Γ, $\Delta\tau$

The steady-state strength for both aging and slip law is given by:

$$\tau_{ss}(V) = \sigma\left(f_0 + (a-b)\ln\frac{V}{V*}\right), \tag{30}$$

so that the stress drop within a crack can be written as (Rubin & Ampuero, 2005)

$$\Delta\tau = \tau_r - \tau_0 = \sigma(b-a)\ln\frac{V}{V_{bg}} \tag{31}$$

where V_{bg} is a hypothetical slip velocity that corresponds to the background stress: $\tau_{ss}(V_{bg}) = \tau_0$. The fracture energy for aging and slip laws were derived by Rubin and Ampuero (2005) and Ampuero and Rubin (2008) respectively. Assuming steady-state within the crack, they are given by

$$\Gamma_{AL} = b\sigma d_c\left(\ln\frac{V\theta_i}{d_c}\right)^2, \tag{32}$$

$$\Gamma_{SL} = b\sigma d_c\ln\frac{V\theta_i}{d_c}. \tag{33}$$

We seek to express Γ and $\Delta\tau$ as a function of the normalized rupture velocity, $\tilde{v}_r \equiv v_r/v_f$. The rupture velocity is related to slip velocity: $v_r \approx (\mu/\Delta\tau_{p-r})V$, where $\Delta\tau_{p-r}$ is the peak-to-residual stress, so we can rewrite eqs. 31, 33 as

$$\Delta\tau = \sigma(a-b)\ln\frac{\tilde{v}}{\tilde{v}_{bg}}, \tag{34}$$

$$\Gamma_{AL} = \frac{b\sigma d_c}{2}\left[\ln\left(\frac{\tilde{v}_r}{\tilde{v}_c}\right)\right]^2, \tag{35}$$

$$\Gamma_{SL} = b\sigma d_c \ln\left(\frac{\tilde{v}_r}{\tilde{v}_c}\right) \tag{36}$$

with $\tilde{v}_{bg} = V_{bg}/V_f$, and $\tilde{v}_c = d_c/(\theta_i V_f)$, where V_f is the slip velocity corresponding to the limit rupture velocity v_f, of the order of the seismic slip velocity. Rubin and Ampuero (2005) observed that $\theta_i/d_c > V_{bg}$ in aging law simulations, which implies $v_c > v_{bg}$. Plugging this expression into eq. 5 we obtain

$$r = \frac{\pi/4}{1-\tilde{v}_r}\frac{\mu' b d_c}{\sigma(b-a)^2}\left[\frac{\ln\tilde{v}_r/\tilde{v}_c}{\ln\tilde{v}_r/\tilde{v}_{bg}}\right]^2 = \frac{R_\infty}{1-\tilde{v}}\left[\frac{\ln\tilde{v}_r/\tilde{v}_c}{\ln\tilde{v}_r/\tilde{v}_{bg}}\right]^2 \tag{37}$$

for the aging law and

$$r = \frac{\pi/2}{1-\tilde{v}_r}\frac{\mu' b d_c}{\sigma(b-a)^2}\frac{\ln\tilde{v}_r/\tilde{v}_c}{(\ln\tilde{v}_r/\tilde{v}_{bg})^2} = \frac{2R_\infty}{1-\tilde{v}_r}\frac{\ln\tilde{v}_r/\tilde{v}_c}{(\ln\tilde{v}_r/\tilde{v}_{bg})^2} \tag{38}$$

for the slip law, where R_∞ is the nucleation length derived by (Rubin & Ampuero, 2005) for the aging law, using static energy balance and noting that for $V \gg \theta_i, V_{bg}$ the term in square brackets tends to 1:

$$R_\infty = \frac{\pi}{4}\frac{b}{(b-a)^2}\frac{\mu' d_c}{\sigma}. \tag{39}$$

B Appendix: Rupture arrest

The fracture mechanics criteria in section 2 can also be applied to rupture arrest. I assume that the region outside an asperity of radius R experiences a stress increase $\Delta\tau_{out}$ during dynamic rupture (due, for example, to velocity-strengthening friction), adding a negative term to the stress intensity factor (Tada, Paris, & Irwin, 2000):

$$K(r) = K^+(r) + K^-(r), \tag{40}$$

with

$$K^+(r) = 2\Delta\tau\sqrt{\frac{r}{\pi}} \tag{41}$$

$$K^-(r) = 2(\Delta\tau_{out} - \Delta\tau)\sqrt{\frac{r^2 - R^2}{r\pi}}, \tag{42}$$

$$\tag{43}$$

where $K^+(r)$ is the SIF due to a stress drop over the entire crack and $K^-(r)$ is the SIF due to an additional stress drop over the region $R \le r \le R_f$ where R_f is the final radius. For the numerical simulations used here (Appendix D), $(a-b)_{VS} = -(a-b)_{VW}$ so that $\Delta\tau_{out} = -\Delta\tau$. Plugging eq. 40 into 6 and solving for rupture velocity yields:

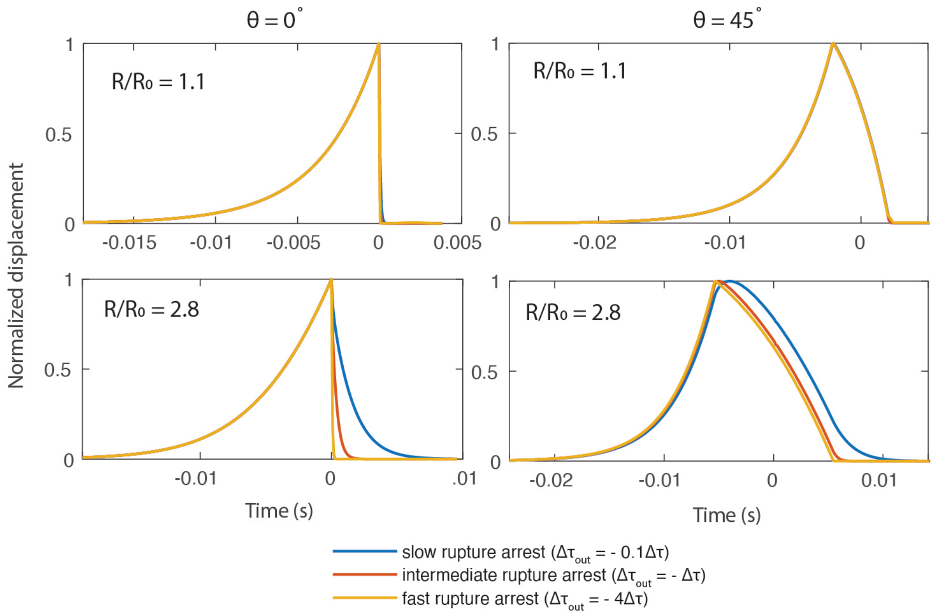

Figure A1: Examples of normalized far-field displacement pulses (S-waves) for two values of R/R_0 and θ, with $c_s = 3600$m/s, $R_0 = 10$m. The deceleration seen for $\theta = 0$ is due to rupture arrest, which is caused by a stress increase in the region $r > R$; the amplitude of this stress increase determines the arrest duration indicated by different colors.

$$\frac{v_r(r)}{v_f} = 1 - \left(\sqrt{\tilde{r}} + \sqrt{\frac{\tilde{r}^2 - \tilde{R}^2}{\tilde{r}}}\right)^{-2}, \tag{44}$$

where $\tilde{r} = r/R_0$, $\tilde{R} = R/R_0$. I solve for rupture velocity as a function of time with the Matlab function `ode45`. The corresponding far-field pulses are shown in Fig. A1.

C Appendix: Pulses and source spectra for $\theta \neq 0$

Sato (1994) derived a surprisingly simple result to compute far-field displacement from circular sources propagating with variable rupture velocity. Let $T(r)$ be the time at which the rupture front reaches radius r, and define the quantities

$$T_a(r) = T(r) - r\sin\theta/c \tag{45}$$

$$T_b(r) = T(r) + r\sin\theta/c, \tag{46}$$

representing the range of arrival times for pulses emitted as the rupture grows from r to $r + dr$. The moment rate function is given by (Sato, 1994)

$$\dot{M}_c(t) = \frac{\pi\mu c a}{2\sin\theta}\left\{R_a(t)^2 - R_b(t)^2\right\}, \tag{47}$$

where R_a, R_b are the solution to $T_a(r) = t$ and $T_b(r) = t$ respectively and a a constant given by

$$a = \left(\frac{24}{7\pi}\right)\left(\frac{\Delta\tau}{\mu}\right). \tag{48}$$

Here I seek an analytical solution for small sources, for the constant Γ model. Writing $R_a = R_0 + l_a$ and $R_b = R_0 + l_b$ and taking $l_{a,b} \ll R_0$, to first order we have: $R_a^2 - R_b^2 \approx 2R_0(l_a - l_b)$. At short times ($t \ll t_0$) the crack radius given by eq. 15 can be approximated as

$$r = R_0 + l_0 e^{t/t_0}, \tag{49}$$

where $l_0 = R_0\epsilon$ is defined as the radius in excess of R_0 at $t = 0$ (which can be arbitrarily small, and is used for mathematical convenience as explained in section 2). Inverting eq. 49 to obtain $T(r)$ and combining with eq. 46 gives

$$l_a(t) = \begin{cases} l_0 e^{t/t_0} e^{\Theta} & t \leq t_a \\ R - R_0 & t > t_a, \end{cases} \tag{50}$$

with $\Theta = R\sin(\theta)/ct_0$ and t_a the arrival time of the stopping phase from the nearest end of the source:

$$t_a = t_0\left[\ln\left(\frac{R - R_0}{l_0}\right) - \Theta\right]. \tag{51}$$

Similarly, l_b is given by

$$l_b(t) = \begin{cases} l_0 e^{t/t_0} e^{-\Theta} & t \leq t_b \\ R - R_0 & t > t_b, \end{cases} \tag{52}$$

with

$$t_b = t_0\left[\ln\left(\frac{R - R_0}{l_0}\right) + \Theta\right]. \tag{53}$$

The moment rate function is proportional to $l_a - l_b$, which reaches its maximum value at $t = t_a$:

$$(l_a - l_b)_{max} = l_0 e^{t_a/t_0}\left(e^{\Theta} - e^{-\Theta}\right). \tag{54}$$

For convenience, we define $t' = t - t_a$ so that $t' = 0$ corresponds to the peak of $\dot{M}_c(t)$ and obtain the following expression for the normalized source time function:

$$\frac{M_c(t')}{\dot{M}_c(0)} = \frac{l_a - l_b}{(l_a - l_b)_{max}} = \begin{cases} e^{t'/t_0} & t' < 0 \\ \dfrac{e^{\Theta} - e^{-\Theta} e^{t'/t0}}{e^{\Theta} - e^{-\Theta}} & 0 \leq t' < \Delta T \\ 0 & \Delta T \leq t \end{cases} \tag{55}$$

with $\Delta T = T_b(R) - T_a(R) = 2R\sin\theta/c = 2\Theta t_0$, and

$$\dot{M}_c(0) = \frac{\pi\mu c a}{\sin\theta} R_0(R - R_0)\left(1 - e^{-2\Theta}\right). \tag{56}$$

As before, I define the source duration as the time in which the displacement pulse exceeds a fraction ϕ of the maximum value, and use eq. 55 to obtain the following expression for the pulse duration:

$$T = t_0\left[\ln\left(\frac{1}{\phi}\right) + \ln\left(\frac{e^{\Theta} - 2\phi\sinh\Theta}{e^{-\Theta}}\right)\right]. \tag{57}$$

Taking the Fourier transform of eq. 55, and reintroducing the constants in eq. 17 yields the following source spectrum:

$$|\dot{M}_c(\omega)| = \frac{48\Delta\tau}{7}(R - R_0)R_0 R \ \mathrm{sinc}\left(\frac{\omega R\sin\theta}{c}\right)\frac{1}{\sqrt{\omega^2 t_0^2 + 1}}. \tag{58}$$

D Appendix: Dynamic rupture simulations

I run fully dynamic simulations using the boundary integral code *BICyclE* (Lapusta, Rice, Ben-Zion, & Zheng, 2000; Lapusta & Liu, 2009). The following equation of motion governs fault slip:

$$\tau_{el}(\mathbf{x}) - \tau_f(\mathbf{x}) = \frac{\mu}{2c_s}V(\mathbf{x}), \tag{59}$$

where μ is the shear modulus, τ_f the frictional resistance, τ_{el} the shear stress due to remote loading and elastodynamic stress interactions between elements, and the term on the right hand side represents radiation damping (Rice, 1993).

Frictional resistance is controlled by rate-state friction with the aging law (section 2.0.1) with the following parameters: $d_c = 10^{-4}$m, $\sigma = 50$MPa, $V^* = 10^{-6}$m/s, $f_0 = 0.6$. With elastic parameters $\mu = 30$GPa, $\nu = 0.25$, this gives a nucleation length $R_\infty = 38$m and 50m for antiplane and plane strain respectively. The model set up is similar to Chen and Lapusta (2009): I impose velocity weakening frictional parameters ($a - b = -0.005$, $b = 0.02$) within a circular asperity, and velocity strengthening parameters ($a - b = 0.005$) in a square region surrounding it. The fault is loaded by a velocity boundary condition $v = 10^{-9}$m/s. To minimize edge effects, the creeping region is at least 3 times larger than the asperity.

Data and Resources

All data used in this paper came from published sources listed in the references.

Acknowledgments

I would like to thank Nadia Lapusta for sharing the *BICyclE* code and Valère Lambert for helping set up the simulations. I am grateful to Paul Segall, Rachel Abercrombie and Victor Tsai for stimulating discussions on these topics, and to the editor and two anonimous reviewers for comments that significantly improved the manuscript. This project was supported by NEHRP grant G19AP00020.

References

Abercrombie, R. E. (1995). Earthquake source scaling relationships from -1 to 5 M_l using seismograms recorded at 2.5-km depth. *Journal of Geophysical Research*, *100*(B12), 24015–24036.

Abercrombie, R. E. (2021, May). Resolution and uncertainties in estimates of earthquake stress drop and energy release. *Philosophical Transactions of the Royal Society A: Mathematical, Physical and Engineering Sciences*, *379*(2196), 20200131. Retrieved 2022-03-09, from `https://royalsocietypublishing.org/doi/10.1098/rsta.2020.0131` (Publisher: Royal Society) doi: 10.1098/rsta.2020.0131

Abercrombie, R. E., & Rice, J. R. (2005, August). Can observations of earthquake scaling constrain slip weakening? *Geophysical Journal International*, *162*(2), 406–424. Retrieved 2022-08-19, from `https://academic.oup.com/gji/article-lookup/doi/10.1111/j.1365-246X.2005.02579.x` doi: 10.1111/j.1365-246X.2005.02579.x

Aki, K. (1967). Scaling law of seismic spectrum. *Journal of Geophysical Research*, *72*(4), 1217–1231. (ISBN: 0148-0227) doi: 10.1029/JZ072i004p01217

Aki, K., & Richards, P. (1980). *Quantitative Seismology: Theory and Methods* (W. H. Freeman, Ed.). New York.

Ampuero, J., & Rubin, A. (2008). Earthquake nucleation on rate and state faults–Aging and slip laws. *Journal of Geophysical Research: Solid Earth*, *113*(August 2007), 1–61. Retrieved from `http://onlinelibrary.wiley.com/doi/10.1029/2007JB005082/full` doi: 10.1029/2007JB005082

Andrews, D. J. (1976, July). Rupture propagation with finite stress in antiplane strain. *Journal of Geophysical Research*, *81*(20), 3575–3582. Retrieved 2022-08-25, from `http://doi.wiley.com/10.1029/JB081i020p03575` doi: 10.1029/JB081i020p03575

Atkinson, G. M., & Beresnev, I. (1997, January). Don't Call it Stress Drop. *Seismological Research Letters*, *68*(1), 3–4. Retrieved 2022-01-14, from `https://pubs.geoscienceworld.org/srl/article/68/1/3-4/142155` doi: 10.1785/gssrl.68.1.3

Baltay, A., Ide, S., Prieto, G., & Beroza, G. (2011). Variability in earthquake stress drop and apparent stress. *Geophysical Research Letters*, *38*(6). Retrieved 2022-03-15, from `https://onlinelibrary.wiley.com/doi/abs/10.1029/2011GL046698` (_eprint: https://onlinelibrary.wiley.com/doi/pdf/10.1029/2011GL046698) doi: 10.1029/2011GL046698

Barry, D., Parlange, J.-Y., Sander, G., & Sivaplan, M. (1993, February). A class of exact solutions for Richards' equation. *Journal of Hydrology*, *142* (1-4), 29–46. Retrieved 2022-08-15, from `https://linkinghub.elsevier.com/retrieve/pii/002216949390003R` doi: 10.1016/0022-1694(93)90003-R

Bindi, D., Spallarossa, D., Picozzi, M., & Morasca, P. (2020, July). Reliability of Source Parameters for Small Events in Central Italy: Insights from Spectral Decomposition Analysis Applied to Both Synthetic and Real Data. *Bulletin of the Seismological Society of America*, *110* (6), 3139–3157. Retrieved 2022-03-09, from `https://doi.org/10.1785/0120200126` doi: 10.1785/0120200126

Boatwright, J. (1978, August). Detailed spectral analysis of two small New York state earthquakes. *Bulletin of the Seismological Society of America*, *68* (4), 1117–1131. Retrieved 2022-08-28, from `https://doi.org/10.1785/BSSA0680041117` doi: 10.1785/BSSA0680041117

Boatwright, J. (1980, February). A spectral theory for circular seismic sources; simple estimates of source dimension, dynamic stress drop, and radiated seismic energy. *Bulletin of the Seismological Society of America*, *70* (1), 1–27. Retrieved 2022-03-11, from `https://doi.org/10.1785/BSSA0700010001` doi: 10.1785/BSSA0700010001

Bouchon, M., Karabulut, H., Aktar, M., Özalaybey, S., Schmittbuhl, J., & Bouin, M. P. (2011). Extended nucleation of the 1999 Mw 7.6 Izmit earthquake. *Science*, *331* (6019), 877–880. (ISBN: 1095-9203 (Electronic)\r0036-8075 (Linking)) doi: 10.1126/science.1197341

Brune, J. N. (1970). Tectonic stress and the spectra of seismic shear waves from earthquakes. *Journ. Geophys. Res.*, *75* (26).

Campillo, M., & Ionescu, I. R. (1997, September). Initiation of antiplane shear instability under slip dependent friction. *Journal of Geophysical Research: Solid Earth*, *102* (B9), 20363–20371. Retrieved 2022-08-25, from `http://doi.wiley.com/10.1029/97JB01508` doi: 10.1029/97JB01508

Cattania, C., & Segall, P. (2019). Crack models of repeating earthquakes predict observed moment-recurrence scaling. *Journ. Geophys. Res.*, *124* (1), 476–503. Retrieved 2019-07-17, from `https://agupubs.onlinelibrary.wiley.com/doi/abs/10.1029/2018JB016056` doi: 10.1029/2018JB016056

Chen, T., & Lapusta, N. (2009). Scaling of small repeating earthquakes explained by interaction of seismic and aseismic slip in a rate and state fault model. *Journal Geophys. Res.*, *114*, 1–12. doi: 10.1029/2008JB005749

Dieterich, J. H. (1992). Earthquake nucleation on faults with rate-and state-dependent strength. *Tectonophysics*, *211* (1-4), 115–134. (ISBN: 0040-1951) doi: 10.1016/0040-1951(92)90055-B

Dieterich, J. H. (1994). A constitutive law for rate of earthquake production and its application to earthquake clustering. *Journal of Geophysical Research*, *99* (B2), 2601–2618.

Dieterich, J. H., & Linker, M. F. (1992). Fault stability under conditions of variable normal stress.

Geophysical Research Letters, *19*(16), 1691–1694. doi: 10.1029/92GL01821

Eshelby, J. (1957). Determination of the elastic field of an ellipsoidal inclusion, and related problems. *Proceedings of the Royal Society of London*. (arXiv: 1011.1669v3 ISBN: 00804630) doi: 10.1098/rspa.1957.0133

Freund, L. B. (1990). *Dynamic Fracture Mechanics*. Cambridge Monographs on Mechanics. Retrieved from `https://www.cambridge.org/core/books/dynamic-fracture-mechanics/4518586440239B156F0C8AD8911E2` doi: 10.1017/CBO9780511546761

Harrington, R. M., & Brodsky, E. E. (2009). Source duration scales with magnitude differently for earthquakes on the San Andreas fault and on secondary faults in Parkfield, California. *Bulletin of the Seismological Society of America*, *99*(4), 2323–2334. (ISBN: 0037-1106) doi: 10.1785/0120080216

Ide, S., Beroza, G. C., Prejean, S. G., & Ellsworth, W. L. (2003). Apparent break in earthquake scaling due to path and site effects on deep borehole recordings. *Journal of Geophysical Research: Solid Earth*, *108*(B5). Retrieved from `http://doi.wiley.com/10.1029/2001JB001617` (ISBN: 0148-0227) doi: 10.1029/2001JB001617

Imanishi, K., & Uchide, T. (2017). Non-self-similar source property for microforeshocks of the 2014 Mw 6.2 Northern Nagano, central Japan, earthquake. *Geophysical Research Letters*, *44*(11), 5401–5410. doi: 10.1002/2017GL073018

Kanamori, H., & Rivera, L. (2004, February). Static and Dynamic Scaling Relations for Earthquakes and Their Implications for Rupture Speed and Stress Drop. *Bulletin of the Seismological Society of America*, *94*(1), 314–319. Retrieved 2022-03-09, from `https://doi.org/10.1785/0120030159` doi: 10.1785/0120030159

Kaneko, Y., & Ampuero, J.-P. (2011, November). A mechanism for preseismic steady rupture fronts observed in laboratory experiments: MODELING PRESEISMIC STEADY RUPTURE. *Geophysical Research Letters*, *38*(21), n/a–n/a. Retrieved 2022-08-29, from `http://doi.wiley.com/10.1029/2011GL049953` doi: 10.1029/2011GL049953

Kaneko, Y., Nielsen, S. B., & Carpenter, B. M. (2016, August). The onset of laboratory earthquakes explained by nucleating rupture on a rate-and-state fault: NUCLEATION OF LABORATORY EARTHQUAKES. *Journal of Geophysical Research: Solid Earth*, *121*(8), 6071–6091. Retrieved 2022-08-29, from `http://doi.wiley.com/10.1002/2016JB013143` doi: 10.1002/2016JB013143

Kaneko, Y., & Shearer, P. M. (2014). Seismic source spectra and estimated stress drop derived from cohesive-zone models of circular subshear rupture. *Geophysical Journal International*, *197*(2), 1002–1015. doi: 10.1093/gji/ggu030

Kaneko, Y., & Shearer, P. M. (2015). Variability of seismic source spectra, estimated stress drop, and radiated energy, derived from cohesive-zone models of symmetrical and asymmetrical circular and elliptical ruptures. *Journal of Geophysical Research B: Solid Earth*, *120*(2), 1053–1079. (ISBN:

0148-0227) doi: 10.1002/2014JB011642

Keilis-Borok, V. (1959, November). On estimation of the displacement in an earthquake source and of source dimensions. *Annals of Geophysics*, *12*(2), 205–214. Retrieved 2022-08-15, from https://www.annalsofgeophysics.eu/index.php/annals/article/view/5718 (Number: 2) doi: 10.4401/ag-5718

Kwiatek, G., & Ben-Zion, Y. (2013). Assessment of P and S wave energy radiated from very small shear-tensile seismic events in a deep South African mine. *Journal of Geophysical Research: Solid Earth*, *118*(7), 3630–3641. Retrieved 2022-03-15, from https://onlinelibrary.wiley.com/doi/abs/10.1002/jgrb.50274 (_eprint: https://onlinelibrary.wiley.com/doi/pdf/10.1002/jgrb.50274) doi: 10.1002/jgrb.50274

Lapusta, N., & Liu, Y. (2009). Three-dimensional boundary integral modeling of spontaneous earthquake sequences and aseismic slip. *Journal of Geophysical Research: Solid Earth*, *114*(B9). Retrieved 2020-05-12, from http://agupubs.onlinelibrary.wiley.com/doi/abs/10.1029/2008JB005934 (_eprint: https://onlinelibrary.wiley.com/doi/pdf/10.1029/2008JB005934) doi: 10.1029/2008JB005934

Lapusta, N., Rice, J. R., Ben-Zion, Y., & Zheng, G. (2000, October). Elastodynamic analysis for slow tectonic loading with spontaneous rupture episodes on faults with rate- and state-dependent friction. *Journal of Geophysical Research: Solid Earth*, *105*(B10). Retrieved 2019-02-15, from http://doi.wiley.com/10.1029/2000JB900250 (Publisher: John Wiley & Sons, Ltd) doi: 10.1029/2000JB900250

Latour, S., Schubnel, A., Nielsen, S., Madariaga, R., & Vinciguerra, S. (2013, October). Characterization of nucleation during laboratory earthquakes. *Geophysical Research Letters*, *40*(19), 5064–5069. Retrieved 2022-08-25, from https://onlinelibrary.wiley.com/doi/abs/10.1002/grl.50974 doi: 10.1002/grl.50974

Leeman, J. R., Saffer, D. M., Scuderi, M. M., & Marone, C. (2016). Laboratory observations of slow earthquakes and the spectrum of tectonic fault slip modes. *Nat Commun*, *7*, 11104. Retrieved from http://www.ncbi.nlm.nih.gov/pubmed/27029996 (Publisher: Nature Publishing Group ISBN: 2041-1723 (Electronic)\r2041-1723 (Linking)) doi: 10.1038/ncomms11104

Lengliné, O., Lamourette, L., Vivin, L., Cuenot, N., & Schmittbuhl, J. (2014). Fluid-induced earthquakes with variable stress drop. *Journal of Geophysical Research: Solid Earth*, *119*(12), 8900–8913. Retrieved 2022-03-09, from https://onlinelibrary.wiley.com/doi/abs/10.1002/2014JB011282 (_eprint: https://onlinelibrary.wiley.com/doi/pdf/10.1002/2014JB011282) doi: 10.1002/2014JB011282

Lin, Y.-Y., & Lapusta, N. (2018). Microseismicity Simulated on Asperity-Like Fault Patches: On Scaling of Seismic Moment With Duration and Seismological Estimates of Stress Drops. *Geophysical Research Letters*, *45*(16), 8145–8155. Retrieved 2022-03-22, from https://onlinelibrary.wiley.com/doi/abs/10.1029/2018GL078650 (_eprint: https://onlinelibrary.wiley.com/doi/pdf/10.1029/2018GL078650) doi: 10.1029/2018GL078650

Lin, Y. Y., Ma, K. F., Kanamori, H., Alex Song, T. R., Lapusta, N., & Tsai, V. C. (2016). Evidence for non-self-similarity of microearthquakes recorded at a Taiwan borehole seismometer array. *Geophysical Journal International*, *206*(2), 757–773. doi: 10.1093/gji/ggw172

Madariaga, R. (1976). Dynamics of an expanding circular fault. *Bulletin of the Seismological Society of America*, *66*(3), 639–666. Retrieved from http://bssa.geoscienceworld.org/content/66/3/639.abstract (ISBN: 0037-1106)

Malagnini, L., Scognamiglio, L., Mercuri, A., Akinci, A., & Mayeda, K. (2008). Strong evidence for non-similar earthquake source scaling in central Italy. *Geophysical Research Letters*, *35*(17). Retrieved 2022-03-09, from https://onlinelibrary.wiley.com/doi/abs/10.1029/2008GL034310 (_eprint: https://onlinelibrary.wiley.com/doi/pdf/10.1029/2008GL034310) doi: 10.1029/2008GL034310

Marone, C. (1998, May). Laboratory-derived friction laws and their application to seismic faulting. *Annual Review of Earth and Planetary Sciences*, *26*(1), 643–696. Retrieved from http://www.annualreviews.org/doi/abs/10.1146/annurev.earth.26.1.643 doi: 10.1146/annurev.earth.26.1.643

Mayeda, K., Malagnini, L., & Walter, W. R. (2007). A new spectral ratio method using narrow band coda envelopes: Evidence for non-self-similarity in the Hector Mine sequence. *Geophysical Research Letters*, *34*(11). Retrieved 2022-03-09, from https://onlinelibrary.wiley.com/doi/abs/10.1029/2007GL030041 (_eprint: https://onlinelibrary.wiley.com/doi/pdf/10.1029/2007GL030041) doi: 10.1029/2007GL030041

McLaskey, G. C. (2019, December). Earthquake initiation from laboratory observations and implications for foreshocks. *Journal of Geophysical Research: Solid Earth*, 2019JB018363. Retrieved 2019-12-20, from https://onlinelibrary.wiley.com/doi/abs/10.1029/2019JB018363 doi: 10.1029/2019JB018363

Ohnaka, M., & Shen, L.-f. (1999, January). Scaling of the shear rupture process from nucleation to dynamic propagation: Implications of geometric irregularity of the rupturing surfaces. *Journal of Geophysical Research: Solid Earth*, *104*(B1), 817–844. Retrieved 2022-08-25, from http://doi.wiley.com/10.1029/1998JB900007 doi: 10.1029/1998JB900007

Palmer, A., & Rice, J. (1973, April). The growth of slip surfaces in the progressive failure of over-consolidated clay. *Proceedings of the Royal Society of London. A. Mathematical and Physical Sciences*, *332*(1591), 527–548. Retrieved 2022-08-25, from https://royalsocietypublishing.org/doi/10.1098/rspa.1973.0040 doi:

10.1098/rspa.1973.0040

Rice, J. R. (1993). Spatio-temporal complexity of slip on a fault. *Journal of Geophysical Research*, *98*(B6), 9885. (ISBN: 2156-2202) doi: 10.1029/93JB00191

Rubin, A. M., & Ampuero, J. (2005). Earthquake nucleation on (aging) rate and state faults. *Journal of Geophysical Research*, *110*(2), 1–24. doi: 10.1029/2005JB003686

Ruina, A. (1983). Slip instability and state variable friction law. *J. Geophys. Res.*, *88*, 10359–10370. Retrieved from http://onlinelibrary.wiley.com/doi/10.1029/JB088iB12p10359/abstract (ISBN: 0148-0227) doi: 10.1029/JB088iB12p10359

Sato, T. (1994, August). Seismic radiation from circular cracks growing at variable rupture velocity. *Bulletin of the Seismological Society of America*, *84*(4), 1199–1215. Retrieved 2022-01-14, from https://doi.org/10.1785/BSSA0840041199 doi: 10.1785/BSSA0840041199

Sato, T., & Hirasawa, T. (1973). Body wave spectra from propagating shear cracks. *Journal of Physics of the Earth*, *21*, 415–431. (ISBN: 0022-3743) doi: 10.4294/jpe1952.21.415

Sato, T., & Kanamori, H. (1999, February). Beginning of earthquakes modeled with the Griffith's fracture criterion. *Bulletin of the Seismological Society of America*, *89*(1), 80–93. Retrieved 2022-08-25, from https://pubs.geoscienceworld.org/ssa/bssa/article/89/1/80/120394/Beginning-of-earthquakes-modeled doi: 10.1785/BSSA0890010080

Selvadurai, P. A. (2019). Laboratory Insight Into Seismic Estimates of Energy Partitioning During Dynamic Rupture: An Observable Scaling Breakdown. *Journal of Geophysical Research: Solid Earth*, *124*(11), 11350–11379. Retrieved 2022-03-15, from https://onlinelibrary.wiley.com/doi/abs/10.1029/2018JB017194 (_eprint: https://onlinelibrary.wiley.com/doi/pdf/10.1029/2018JB017194) doi: 10.1029/2018JB017194

Shearer, P. M., Abercrombie, R. E., Trugman, D. T., & Wang, W. (2019). Comparing EGF Methods for Estimating Corner Frequency and Stress Drop From P Wave Spectra. *Journal of Geophysical Research: Solid Earth*, *124*(4), 3966–3986. Retrieved 2022-03-15, from https://onlinelibrary.wiley.com/doi/abs/10.1029/2018JB016957 (_eprint: https://onlinelibrary.wiley.com/doi/pdf/10.1029/2018JB016957) doi: 10.1029/2018JB016957

Tada, H., Paris, P. C., & Irwin, G. R. (2000). *The Stress Analysis of Cracks Handbook*. Hellertown PA: Del Research Corp. doi: 10.1115/1.801535

Trugman, D. T., & Shearer, P. M. (2017). Application of an improved spectral decomposition method to examine earthquake source scaling in Southern California. *Journal of Geophysical Research: Solid Earth*, *122*(4), 2890–2910. Retrieved 2022-03-09, from https://onlinelibrary.wiley.com/doi/abs/10.1002/2017JB013971 (_eprint: https://onlinelibrary.wiley.com/doi/pdf/10.1002/2017JB013971) doi: 10.1002/2017JB013971

Viesca, R. C., & Garagash, D. I. (2015). Ubiquitous weakening of faults due to thermal pressurization.

Nature Geosci, *8*(October). doi: 10.1038/NGEO2554

Wang, H., Ren, Y., Wen, R., & Xu, P. (2019). Breakdown of Earthquake Self-Similar Scaling and Source Rupture Directivity in the 2016–2017 Central Italy Seismic Sequence. *Journal of Geophysical Research: Solid Earth*, *124*(4), 3898–3917. Retrieved 2022-03-09, from `https://onlinelibrary.wiley.com/doi/abs/10.1029/2018JB016543` (_eprint: https://onlinelibrary.wiley.com/doi/pdf/10.1029/2018JB016543) doi: 10.1029/2018JB016543

Wang, Y., & Day, S. M. (2017). Seismic source spectral properties of crack-like and pulse-like modes of dynamic rupture. *Journal of Geophysical Research: Solid Earth*, *122*(8), 6657–6684. doi: 10.1002/2017JB014454

Wolfram Research, I. (2022). *Mathematica Online.* Champaign, Illinois.

Yoshimitsu, N., Kawakata, H., & Takahashi, N. (2014). Magnitude -7 level earthquakes: A new lower limit of self-similarity in seismic scaling relationships. *Geophysical Research Letters*, *41*(13), 4495–4502. Retrieved 2022-03-15, from `https://onlinelibrary.wiley.com/doi/abs/10.1002/2014GL060306` (_eprint: https://onlinelibrary.wiley.com/doi/pdf/10.1002/2014GL060306) doi: 10.1002/2014GL060306

Zollo, A., Orefice, A., & Convertito, V. (2014). Source parameter scaling and radiation efficiency of microearthquakes along the Irpinia fault zone in southern Apennines, Italy. *Journal of Geophysical Research: Solid Earth*, *119*(4), 3256–3275. Retrieved 2022-03-09, from `https://onlinelibrary.wiley.com/doi/abs/10.1002/2013JB010116` (_eprint: https://onlinelibrary.wiley.com/doi/pdf/10.1002/2013JB010116) doi: 10.1002/2013JB010116

Mailing Address

Camilla Cattania
Department of Earth, Atmospheric, and Planetary Sciences
Massachusetts Institute of Technology
77 Massachusetts Ave, 54-418
Cambridge, MA 02139

List of Figures

1 Coordinate system and sketch of rupture propagation. Circular ruptures propagate at variable speed into a region of positive stress drop ($r < R$) and arrest due to a negative stress drop at $r > R$. R_0 is a nucleation radius defined in the text. 3

2 Evolution of rupture velocity with radius for rate-state models with the aging law (left) and slip law (right) for different values of normalized characteristic velocity v_c/v_f; I assumed $v_{bg} = 0.1v_c$ in all cases. Solid lines indicate dynamic models (eq. 10, 11) and dotted lines indicate quasi-static models obtained by setting $v_r/v_f = 0$. For small v_c/v_f, the quasi-static solution approaches R_∞, and dynamic solutions approach the constant model (black). Thin black lines indicate the constant $\Gamma, \Delta\tau$ model shifted along the x-axis, representing the same scaling but with a different nucleation dimension. Numbers indicate the power-law exponent in the relation $v_r \sim r^m$, calculated at $v_r/v_f = 0.01$. 6

3 Normalized far-field displacements observed at $\theta = 0$ for different underlying source models. (a) Sato and Hirasawa (1973) model with constant rupture velocity. (b) kinematic modified model accounting for accelerating rupture, with instantaneous rupture arrest and constant fracture energy and stress drop. (c) kinematic model for rate-state friction with the aging law with $v_c/v_f = 10^{-8}$, $v_{bg}/v_f = 10^{-9}$ (eq. 10). (d) fully dynamic earthquake simulations. Dotted lines are theoretical expressions for $R \approx R_0$ ($u/u_{max} = \exp(-\Delta t/t_0)$). The nucleation length R_0 in panels (b,c) is set to R_∞ (eq. 39) corresponding to the parameters in the simulation (Appendix D). The rupture velocity v_r is equal to the shear wave speed, corresponding to the mode III edge of the rupture. 11

4 Corner frequency and fall-off exponents estimated by fitting a Brune and a Boatwright spectrum to the far-field displacements produced by an event near the nucleation dimension $R = 1.1R_0$ and fast rupture arrest ($\Delta\tau_{out} = -4\Delta\tau$), with $R_0 = 10$m, $v_f = 2880$m/s. (a) Brune (cross) and Boatwright (circle) corner frequencies generally fall between the two theoretical corner frequencies predicted by eq. 25 associated with the rupture acceleration (dotted line) and to the delay between stopping phases (solid line). (b) Spectrum for $\theta = 0°$, close to the expected Boatwright spectrum for $R \approx R_0$, eq. 23. (c) Spectrum for $\theta = 45°$. 13

5 (a) normalized seismic moment vs. normalized radius predicted by the theoretical source model (section 2). The solid and dotted lines indicate analytical results for $R \gg R_0$ (eq. 1) and $R \approx R_0$ (eq. 26). Light blue, solid circles are the $\theta = 0°$; black empty circles for $\theta = 45°$. (b) Measured stress drop vs. earthquake magnitude. 15

6 Far-field displacement durations and seismic moments from Lin et al. (2016), with each color corresponding to a different cluster. Black lines indicate the predicted scaling for sources near the nucleation dimension (eq. 24, 26) with $\theta = 28°$, $v_r = 2505$m/s, $c = 5700$m/s, $\phi = 1/2$ (from Lin et al. (2016)), $\Delta\tau = 3$MPa and $\mu = 30$GPa. The dotted line indicates the classical $T \sim M_0^{1/3}$ scaling for a 3MPa stress drop. 17

7 (a) Normalized seismic moment vs. normalized corner frequency, obtained from the scaling shown in Fig. 5 (lines) with variable nucleation lengths drawn from a Gaussian distribution. The reference corner frequency is defined from eq. 27 such that $\Delta\tau_m(M_{0,ref}, f_{ref}) = \Delta\tau$, with $\Delta\tau$ the nomimal stress drop. (b) Ratio between measured and true stress drop vs. magnitude relative to the reference magnitude. (c) PDF of normalized asperity dimensions (top) and nucleation lengths (bottom). 18

A1 Examples of normalized far-field displacement pulses (S-waves) for two values of R/R_0 and θ, with $c_s = 3600$m/s, $R_0 = 10$m. The deceleration seen for $\theta = 0$ is due to rupture arrest, which is caused by a stress increase in the region $r > R$; the amplitude of this stress increase determines the arrest duration indicated by different colors. 21